Magnetic Resonance Imaging of Stem Cell Apoptosis in Arthritic Joints with a Caspase Activatable Contrast Agent

Hossein Nejadnik,[†,⊥] Deju Ye,[†,‡,⊥] Olga D. Lenkov,[†] Jessica S. Donig,[†] John E. Martin,[†] Rostislav Castillo,[†] Nikita Derugin,[†] Barbara Sennino,[§] Jianghong Rao,[†,∥] and Heike Daldrup-Link*[,†,∥]

[†]Department of Radiology and Molecular Imaging Program at Stanford (MIPS), Stanford School of Medicine, Stanford, California 94305, United States, [‡]State Key Laboratory of Analytical Chemistry for Life Science, School of Chemistry and Chemical Engineering, Nanjing University, Nanjing 210093, China, and [§]Comprehensive Cancer Center, Cardiovascular Research Institute and Department of Anatomy, University of California at San Francisco, San Francisco, California 94143, United States. [⊥]These authors contributed equally. [∥]These authors contributed as co-senior authors.

ABSTRACT About 43 million individuals in the U.S. encounter cartilage injuries due to trauma or osteoarthritis, leading to joint pain and functional disability. Matrix-associated stem cell implants (MASI) represent a promising approach for repair of cartilage defects. However, limited survival of MASI creates a significant bottleneck for successful cartilage regeneration outcomes and functional reconstitution. We report an approach for noninvasive detection of stem cell apoptosis with magnetic resonance imaging (MRI), based on a caspase-3-sensitive nanoaggregation MRI probe (C-SNAM). C-SNAM self-assembles into nanoparticles after hydrolysis by caspase-3, leading to 90% amplification of ^{1}H MR signal and prolonged *in vivo* retention. Following intra-articular injection, C-SNAM causes significant MR signal enhancement in apoptotic MASI compared to viable MASI. Our results indicate that C-SNAM functions as an imaging probe for stem cell apoptosis in MASI. This concept could be applied to a broad range of cell transplants and target sites.

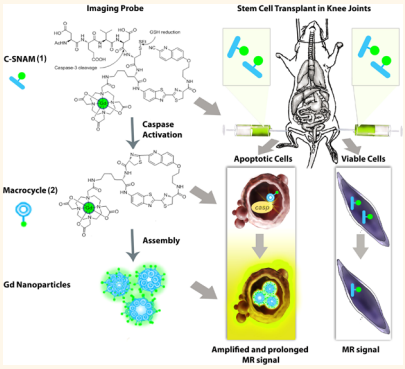

KEYWORDS: stem cell · apoptosis · MRI · molecular imaging · nanoparticles · arthritis

Joint injuries due to trauma or degenerative arthritis result in 44 million outpatient visits and 992 100 hospitalizations each year.[1−3] Cartilage defects are the main source of joint pain and disability in these patients and are difficult to treat because cartilage cannot self-regenerate.[4] Advanced joint injuries are treated with knee replacement procedures, with currently 700 000 procedures per year and 3.48 million annual procedures expected by 2030.[5] The lifetime of an artificial prosthesis is limited to about 10 years due to wear of the implant, and secondary prostheses are often associated with complications.[6−8] It would be better to repair cartilage defects at an early stage, before major joint destruction occurs. New cell therapies based on transplants of autologous chondrocytes, stem cells, or stem-cell-derived chondrocytes provide encouraging results in this regard.[9,10] However, a major barrier for long-term success of stem-cell-mediated cartilage repair is the death of transplanted cells before they can exert their therapeutic effects.

Apoptosis of transplanted stem cells in cartilage defects can be triggered by proinflammatory conditions at the tissue injury site.[11,12] While the *in vitro* environment used to culture stem cells features controlled temperature, steady oxygen levels, constant pH, and rich nutrition conditions, the injury site is usually hypoxic,[13−15] contains high levels of inflammatory mediators,[16] and has limited nutrients.[15] As a result, a large portion of implanted cells undergo programmed cell death[17] and are cleared from the transplantation site by macrophages,[9,11,12] leading to poor tissue repair outcomes.[18] A variety of interventions for improved stem cell survival have been recently proposed, such as growth-factor-enriched biomaterials, genetic vectors for increased expression of survival genes in stem cells, short-term immunosuppression, and apoptotic inhibitors and/or prosurvival factors.[15,19−24] An imaging technique that could visualize stem cell apoptosis directly would greatly enhance our ability to apply

* Address correspondence to h.e.daldrup-link@stanford.edu.

Received for review August 12, 2014 and accepted January 17, 2015.

Published online January 17, 2015
10.1021/nn504494c

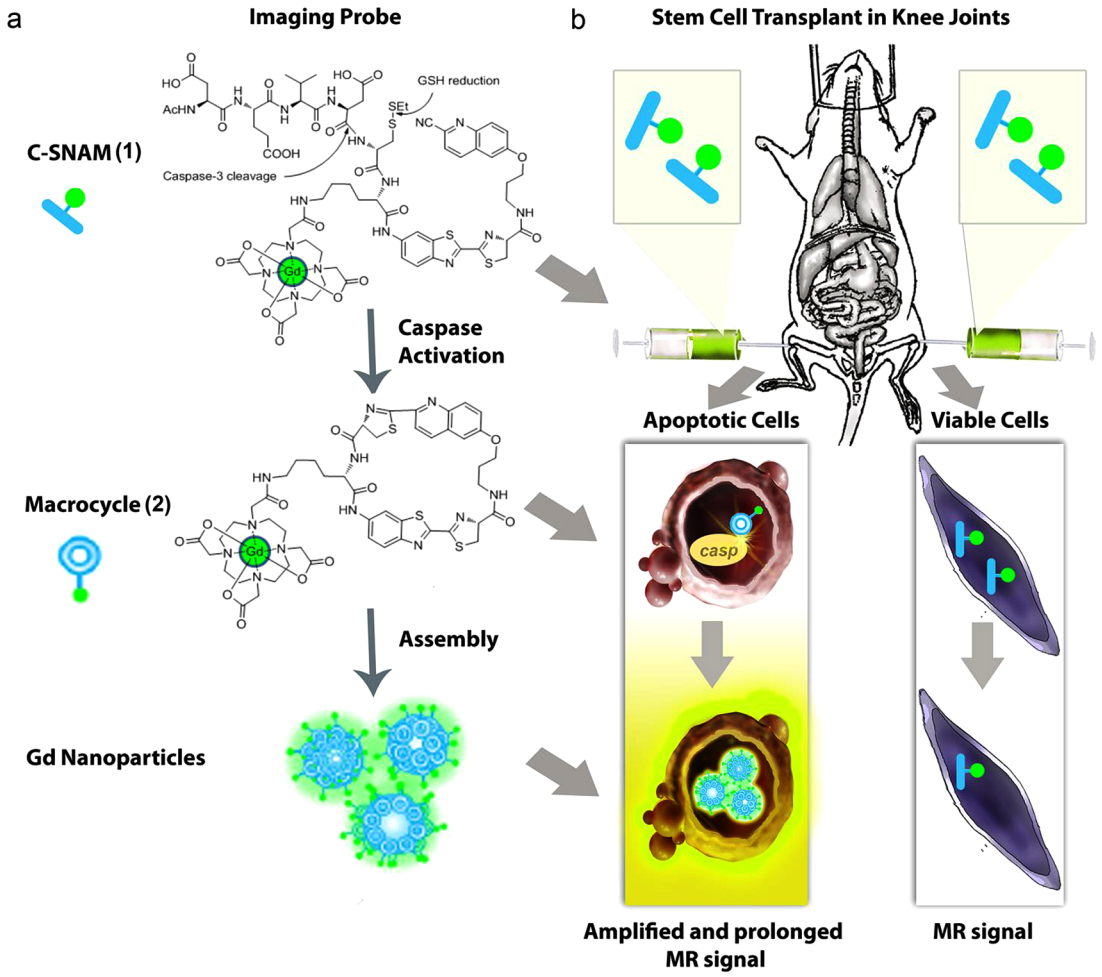

Figure 1. General design and mechanism of action of the caspase-3-sensitive nanoaggregation MRI probe (C-SNAM). (a) Chemical structure of C-SNAM (1). Following disulfide reduction and caspase-3-triggered DEVD peptide cleavage, C-SNAM transforms to a rigid and hydrophobic macrocyclic product 2, through a biocompatible intramolecular cyclization reaction between 2-cyano-6-hydroxyquinoline and D-cysteine residue. The macrocycle 2 will subsequently self-assemble into Gd nanoparticles, leading to an increase in r_1 relaxivity relative to the unactivated probe 1. (b) Corresponding mechanism of action *in vivo*. (1) Intra-articular injection of C-SNAM into rat knee joints with implants of apoptotic and viable stem cells. (2) *In vivo* activation of C-SNAM in apoptotic stem cell transplants through caspase-3-mediated activation. (3) Increased relaxivity and retention effect of GdNPs lead to enhanced MRI signal of apoptotic stem cell transplants.

these interventions at an early time when salvage of cell transplants is still possible.

To address the urgent need of noninvasively detecting transplanted stem cell apoptosis *in vivo*, we developed a new magnetic resonance imaging (MRI) approach by using a gadolinium (Gd)-based contrast agent (caspase-3-sensitive nanoaggregation MRI probe, C-SNAM), which is activated by caspase-3, a common cell apoptosis biomarker.[25] We chose an MRI-detectable biomarker because MRI is the only imaging modality to date that can directly detect cartilage defects *in vivo*.[26,27] Our C-SNAM probe is fundamentally different from previous approaches.[28,29] C-SNAM is a small molecular probe, which can be easily delivered to matrix-associated stem cell implants (MASI) in cartilage defects through intra-articular injection and passive diffusion. Upon caspase-3 activation, C-SNAM is converted into Gd nanoparticles (GdNPs) through *in vivo* self-assembly. This increases its relaxivity (MR signal effect) and prolongs tissue retention in apoptotic MASI, thereby providing enhanced target-to-background contrast. On the basis of this "enhanced relaxivity and retention effect", we postulated that C-SNAM could detect apoptosis of MASI in arthritic joints *in vivo* with MR imaging, providing early, noninvasive diagnosis of failed MASI with sub-millimeter spatial resolution. This new MRI-based imaging approach could facilitate optimizations of MASI strategies, could be broadly applied to a wide variety of stem cell therapies beyond cartilage repair, and, ultimately, could help to improve tissue regeneration outcomes.

RESULTS

Evaluation of Caspase-3 Activatable MRI Probe C-SNAM. We synthesized C-SNAM, a small molecular Gd-chelate, which can be easily delivered to MASI through intra-articular injection and passive diffusion. Figure 1 shows the chemical structure of C-SNAM and illustrates its

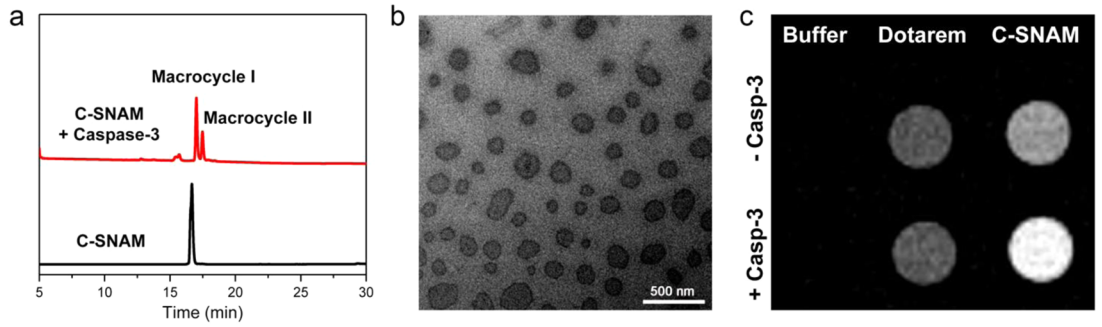

Figure 2. *In vitro* **characterization of C-SNAM. (a) HPLC traces of C-SNAM (black) and the incubation of C-SNAM (200 μM) with recombinant human caspase-3 (50 nM) in the caspase buffer at 37 °C overnight (red). (b) TEM images of GdNPs formed in the solution of C-SNAM (200 μM) following incubation with caspase-3 (50 nM) in caspase buffer (pH 7.4) overnight. Scale bar: 500 nm. (c) T_1-weighted images show brighter MR signal for C-SNAM than other probes upon caspase-3 incubation. C-SNAM and Gd-DOTA (Dotarem) at 200 μM in enzyme reaction buffer were incubated with and without caspase-3 (50 nM) at 37 °C overnight. T_1-weighted FLASH images (TR/TE = 161/6 ms) of the incubation solutions were acquired at 1 T at 37 °C.**

mechanism of action in the presence of caspase-3. Upon activation by caspase-3, the disulfide bond is reduced and the peptide sequence of Asp-Glu-Val-Asp (DEVD) is cleaved, liberating free N-terminal D-cysteine, which is subsequently condensed with 2-cyano-6-hydroxyquinoline intramolecularly to form cyclized products (macrocycles I and II), as detected by high-performance liquid chromatography (HPLC) and high-resolution mass spectroscopic (HRMS) analysis (Figure 2a and Supporting Information Figure S1). Due to the increased rigidity and hydrophobicity of the macrocycles that can contribute to intermolecular interactions (*i.e.*, hydrophobic interactions, $\pi-\pi$ stacking), they further self-assemble into GdNPs under physiological conditions, with diameters ranging from 50 to a few hundred nanometers as detected by dynamic light scattering (DLS) (Supporting Information Figure S2). Transmission electron microscopy measurement (TEM; in Figure 2b) further confirmed the spherical shapes of individual nanoparticles, with size distribution similar to that observed by DLS. Energy-dispersive X-ray (EDX) spectroscopy analysis clearly showed the elemental signals of Gd in the observed nanoparticles on TEM (Supporting Information Figure S3), validating the caspase-3-activated formation of GdNPs through *in situ* self-assembly. Compared to the hydrophilicity and small size of C-SNAM, the self-assembled GdNPs have a much increased size and thus a longer rotational correlation time (τ_R),[30−33] which can remarkably amplify the longitudinal r_1 relaxivity. The r_1 relaxivity of C-SNAM, as determined by *in vitro* MRI measurements at 1 T, was 10.2 ± 1.5 $mM^{-1}\cdot s^{-1}$ and increased to 19.0 ± 0.5 $mM^{-1}\cdot s^{-1}$ after activation by recombinant caspase-3 in enzyme buffer (Figure 1a). This increase of ~90% was statistically significant ($P < 0.05$). The higher r_1 relaxivity of C-SNAM after caspase-3 activation resulted in significantly brighter signal on T_1-weighted MR images relative to C-SNAM or Gd-DOTA (Dotarem) at the same concentration in solution at 1 T (Figure 2c). Therefore, measuring the MRI signal allowed us to differentiate original intact C-SNAM and caspase-3-activated GdNPs.

C-SNAM Detects Stem Cell Apoptosis *in Vitro*. To evaluate the ability of C-SNAM to detect stem cell apoptosis *in vitro*, we incubated viable and mitomycin C (MMC)-pretreated apoptotic rat adipose-derived stem cell (rASC) with increasing concentrations of the C-SNAM probe, followed by MRI, bioluminescence imaging (BLI), and respective quantitative data (Figure 3).

C-SNAM-exposed apoptotic rASCs demonstrated T_1 signals on MR images that were significantly stronger than those of viable rASCs (Figure 3c). Corresponding BLI studies confirmed apoptosis of MMC-exposed cells and unimpaired viability of untreated cells, and respective luminescent signal quantification showed significant apoptosis in MMC-exposed apoptotic rASC ($P < 0.05$, Figure 3d).

T_1 relaxation times of apoptotic rASCs were significantly shorter than relaxation times of viable rASC after incubation with C-SNAM at concentrations of 250 and 500 μM ($p \leq 0.0002$; Figure 4a). Of note, shorter T_1 relaxation times led to an increased MR signal on T_1-weighted MR images. Further increases in C-SNAM concentration did not result in significant differences in MR signal effects between viable and apoptotic rASC, presumably due to a saturation effect. Control experiments with the nonactivatable small molecular Gd-chelate Gd-DOTA did not show any significant difference in T_1 relaxation times between viable and apoptotic rASC ($P > 0.05$; Figure 4d).

Subsequent analysis of the Gd concentrations of the cell samples with inductively coupled plasma mass spectrometry (ICP-MS) revealed significantly higher Gd concentrations in apoptotic rASC than in viable rASC when incubated at 250 and 500 μM probe concentrations. This suggests an increased retention of the probe in apoptotic rASC, due to the caspase-3 activation ($P < 0.001$; Figure 4b). In addition, rASC with equal Gd content showed significantly shorter T_1 relaxation times for apoptotic than for viable cell samples,

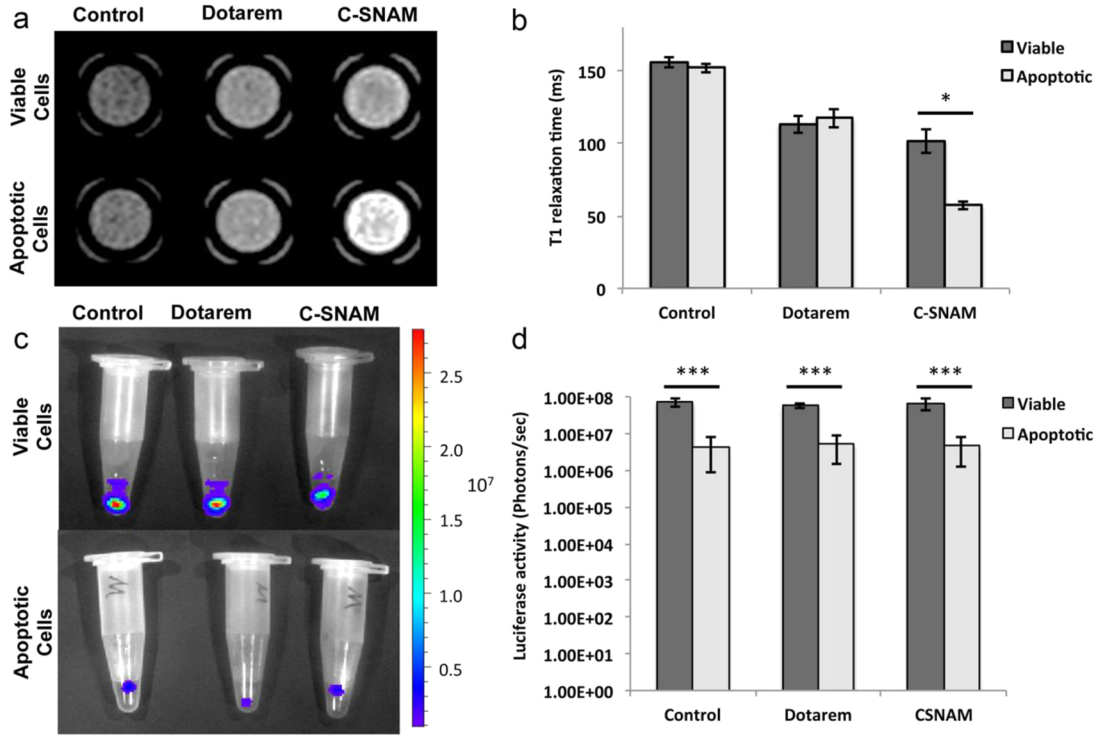

Figure 3. MR imaging and bioluminescence imaging of FLuc-eGFP-transfected rat adipose-derived stem cells. (a) T_1-weighted MR images of 3 $\times$ 10^6 viable and apoptotic FLuc-eGFP-transfected rASCs in PBS (control), 500 μM Dotarem (nonactivatable contrast agent), or 500 μM C-SNAM solution. (b) Corresponding T_1 relaxation times of viable and apoptotic stem cells, displayed as mean data of three experiments in each group with standard errors. *Indicates significant differences between viable and apoptotic cells ($P < 0.05$). (c) Corresponding bioluminescence imaging studies of centrifuged pellets of viable and apoptotic FLuc-eGFP-transfected rASCs in microcentrifuge Eppendorf test tubes. (d) Corresponding luminescent signal of viable and apoptotic rASCs, displayed as mean data of three experiments in each group with standard errors. ***Indicates significant differences between viable and apoptotic cells ($P < 0.001$).

indicating an additional component of contrast agent activation (Figure 4c). In accordance with the T_1 relaxation times measured in Figure 4d, ICP-MS results did not show any significant differences in Gd uptake in viable and apoptotic cells after incubation with Gd-DOTA ($P > 0.05$; Figure 4e).

MMC-treated apoptotic rASCs demonstrated positive caspase-3 immunofluorescent stains, while viable rASCs showed negative stains (Figure 5a). Flow cytometry analysis of caspase-3 expression (FLICA, a fluorescent inhibitor of caspase-3) revealed that ~40% of rASCs contained caspase-3 following MMC treatment (Figure 5b). The quantitative fluorescent caspase-3 assay demonstrated ~4-fold increase in caspase-3 production of apoptotic rASCs when compared to viable rASCs ($P < 0.0001$; Figure 5c).

***In Vivo* Detection of Stem Cell Apoptosis.** *In vivo* MR and optical imaging studies were performed in athymic female Harlan rats at 24 h after transplantation of viable FLuc-eGFP-transduced rASCs into an osteochondral defect of the left distal femur ($n = 5$ knees) and MMC-treated apoptotic FLuc-eGFP-transduced rASCs into an osteochondral defect of the right distal femur ($n = 5$ knees; Figure 1). We chose the highest C-SNAM concentration (500 μM) which showed significant differences in MR signal between viable and apoptotic cells *in vitro* in order to account for a potential dilution of the C-SNAM probe with synovial fluid *in vivo*.

Following intra-articular injection of the C-SNAM probe, MR imaging studies demonstrated an initial positive (bright) enhancement of all joint spaces on T_1-weighted sequences, followed by gradual enhancement of MASI. At 30 min after intra-articular C-SNAM injection, apoptotic MASI demonstrated a markedly stronger signal enhancement than viable MASI (Figure 6a). Accordingly, T_1 relaxation times of apoptotic transplants were significantly shorter compared to viable transplants ($P = 0.0198$). Follow-up MR imaging scans 24 h later demonstrated recovery of the MR signal of both viable and apoptotic implants, confirming elimination of the probe. Corresponding quantitative data revealed no remaining T_1 relaxation time shortening compared to precontrast baseline values ($P > 0.05$; Figure 6b).

Corresponding BLI studies demonstrated a strong bioluminescent signal of all rASC implants immediately after *in vivo* implantation, followed by loss of BLI signal of MMC-treated rASC implants 24 h later (Figure 6c and Supporting Information Figure S4). The MMC-treated apoptotic rASC implants showed a significant decline in bioluminescent signal when compared to contralateral viable rASC implants ($P = 0.002$; Figure 6d).

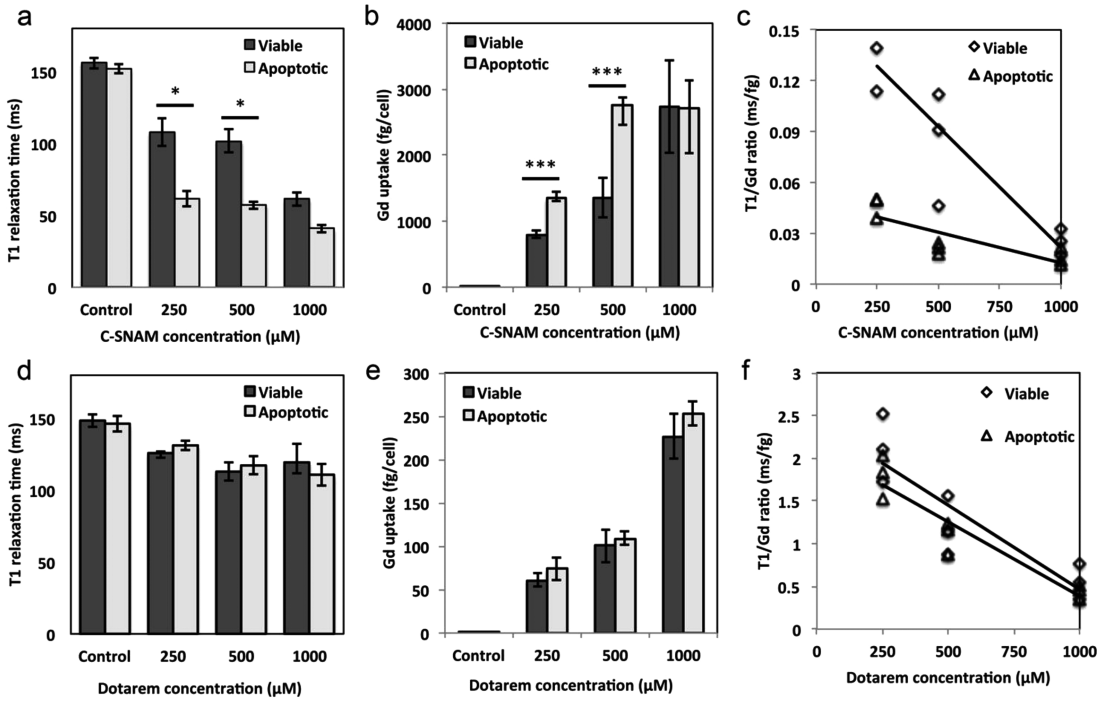

Figure 4. Enhanced relaxivity and retention of C-SNAM in apoptotic rASCs *in vitro*. (a) T_1 relaxation times of viable and apoptotic rASCs after incubation with increasing concentrations of the C-SNAM probe. *Indicates significant differences between viable and apoptotic cells ($P < 0.05$). (b) Corresponding Gd uptake of viable and apoptotic rASCs (***indicates significant differences ($P < 0.001$) between viable and apoptotic cells). (c) Ratio of the T_1 relaxation time/Gd uptake of viable and apoptotic rASCs. (d) T_1 relaxation times of viable and apoptotic rASCs after incubation with increasing concentrations of Gd-DOTA as a nonactivatable control probe. (e) Corresponding Gd uptake of viable and apoptotic rASCs. (f) Ratio of the T_1 relaxation time/Gd uptake of viable and apoptotic rASCs. All data were measured as mean data of three experiments in each group and standard errors.

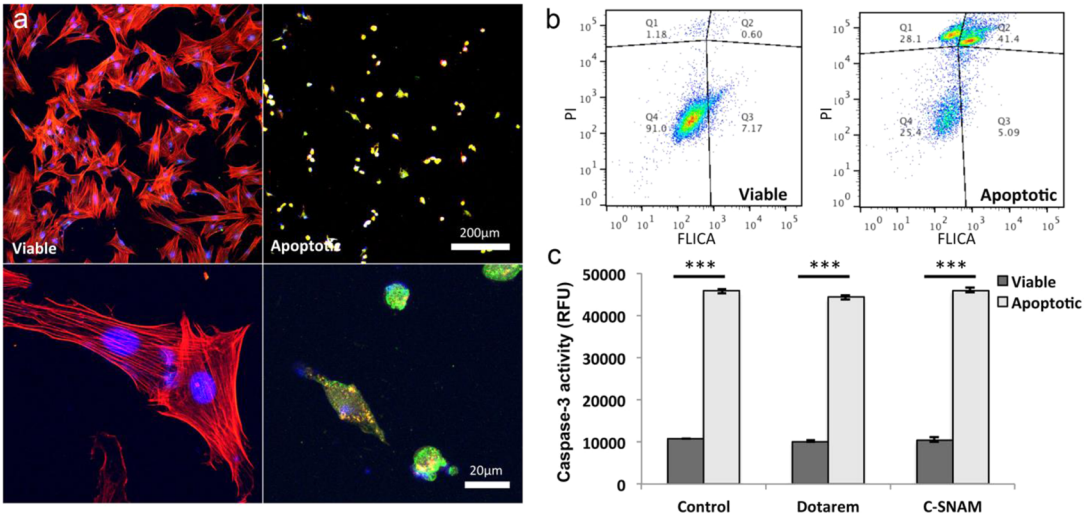

Figure 5. *In vitro* analysis of rASC apoptosis at 24 h after incubation with mitomycin. (a) Confocal microscopy of viable and MMC-treated apoptotic rASCs demonstrates cleaved caspase-3 (green fluorescence indicates activated caspase-3; red fluorescence shows F-actin filaments, and DAPI displays cell nucleus with blue fluorescence). (b) Flow cytometry (ex/em = 488/530) analysis of viable (left panel) and apoptotic rASCs (right panel) which were stained with the FLICA kit (fluorescent inhibitor of caspases). (c) Quantification of cleaved caspase-3 in viable and apoptotic rASCs by the SensoLyte homogenous AMC caspase-3/7 kit. Upon caspase-3/7 cleavage, Ac-DEVD-AMC generates the AMC fluorophore, which has bright blue fluorescence and can be quantified at ex/em = 354 nm/442 nm. Data are displayed as means of three experiments in each group with standard errors. ***Indicates significant differences between viable and apoptotic cells ($P < 0.001$).

Histological immunofluorescent stains against cleaved caspase-3 confirmed the presence of active caspase-3 and increased fluorescence signal in apoptotic MASI compared with viable MASI (Figure 7).

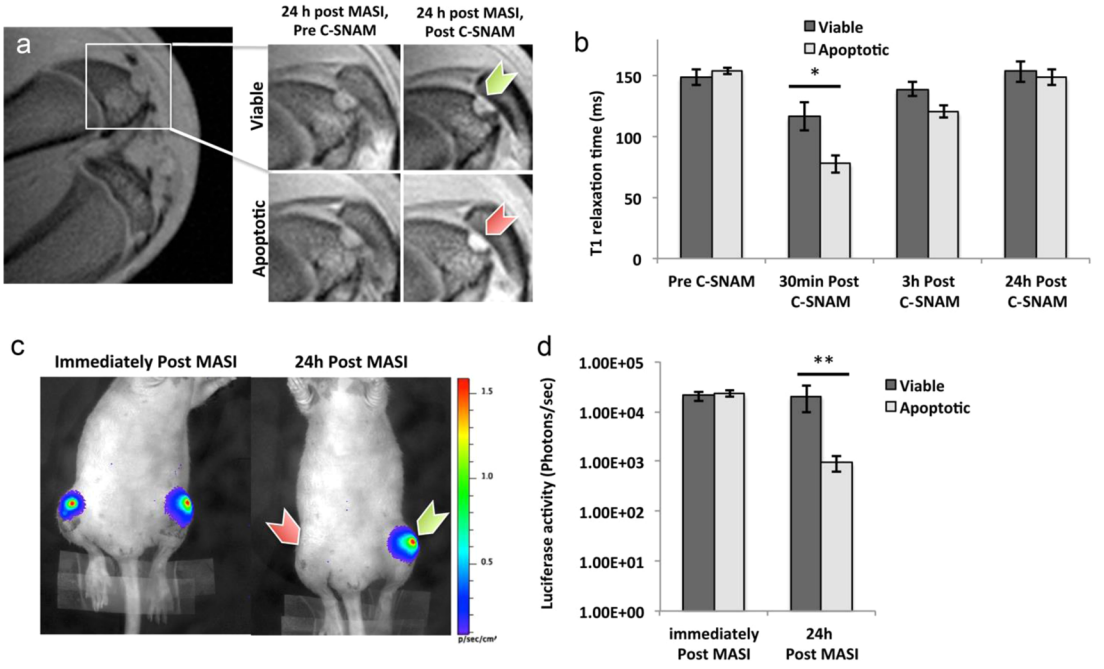

Figure 6. *In vivo* MRI and BLI of viable and apoptotic rASC implants. (a) Representative sagittal MR images of viable rASCs (green arrow) and apoptotic rASCs (red arrow) in an osteochondral defect of representative rat knee joints before and 30 min after intra-articular injection of C-SNAM. (b) Corresponding T_1 relaxation times of viable and apoptotic rASC implants at different time points before and after intra-articular injection of C-SNAM. Data are displayed as means of five experiments in each group with standard errors. *Indicates significant differences between viable and apoptotic cells ($P < 0.05$). (c) *In vivo* BLI of representative viable (green arrow) and apoptotic (red arrow) rASCs immediately and 24 h after MASI implantation. (d) Respective luminescent signal of viable and apoptotic rASCs. Data are displayed as means of five experiments in each group with standard deviation. **Indicates significant differences between viable and apoptotic cells ($P < 0.01$).

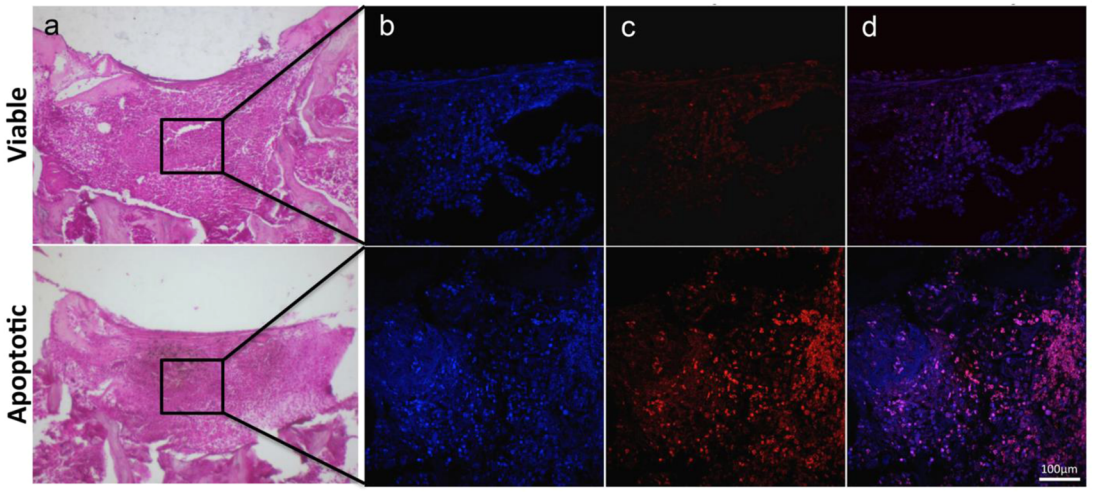

Figure 7. Corresponding histopathology of viable (top row) and apoptotic (low row) rASC implants. (a) H&E stains show MASI implant in the knee joint (b) DAPI stain shows cell nucleus (blue fluorescence), (c) red fluorescence demonstrates cleaved caspase-3 in apoptotic rASCs. (d) Overlay of b and c (scale bar = 100 μm).

DISCUSSION

Our data show that C-SNAM can detect apoptosis of matrix-associated stem cell implants in arthritic joints. C-SNAM enabled noninvasive *in vivo* differentiation of viable and apoptotic stem cell transplants on MR images with subcentimeter anatomical resolution. The information provided by this novel MR molecular imaging probe could be applied to evaluate endogenous or exogenous factors that support stem cell survival *in vivo* and, ultimately, could facilitate the development of stem cell therapies that lead to successful cartilage repair.

Stem cells can regenerate cartilage.[12] However, cartilage defect repair outcomes of transplanted stem cells have been highly variable in animal models. While some groups have reported successful regeneration of

hyaline cartilage, others have reported complications such as fibrous tissue formation and incomplete healing with persisting cartilage defects.[34−37] Cartilage repair outcomes are dependent on survival of the transplanted cells in injured cartilage.[38] One of the main reasons for lack of cartilage repair is cell apoptosis due to pro-inflammatory conditions at the tissue injury site.[11,12,39] Similar problems with apoptosis and loss of transplanted stem cells have also been observed in other disease models, such as stroke, Parkinson's disease, myocardial infarction, muscular dystrophy, and diabetes.[39] An imaging technique that could monitor the viability of transplanted stem cells noninvasively *in vivo* could be broadly applied to facilitate the diagnosis of failed cell therapies and enable corrective actions, such as revision surgery.

Currently, the success of MASI in arthritic patients is determined by the degree of repair of the underlying cartilage defect several months after the surgery, as observed using MRI or arthroscopy.[40,41] However, stem cell death—the most common cause for failed stem cell transplants—typically occurs during the first few weeks after transplantation. There is currently no imaging probe available that can detect cell death directly. Our C-SNAM probe solves this problem, thereby enabling accelerated detection of failed cell transplants.

Our group has used iron oxide nanoparticles for stem cell detection with MRI.[42−44] These studies show that the signal kinetics of iron oxide nanoparticle-labeled cells over time can provide some information about the viability of the transplanted cells. The MR signal of apoptotic iron oxide-labeled cells in cartilage defects disappears faster than in iron oxide-labeled viable cells because macrophages from bone marrow migrate into the defect, phagocytose the iron-labeled cells, and metabolize the internalized iron faster than the original stem cells.[45] However, this approach requires direct labeling of transplanted stem cells and at least two serial MRI scans.[46−48] In contrast, our method of using an intra-articular injection of caspase-3 activatable Gd-chelate to diagnose MASI apoptosis does not require any manipulation of the transplanted stem cells and could be performed with one MRI exam.

Previous approaches for *in vivo* detection of apoptosis have utilized radiotracers for single-photon emission computed tomography or positron emission tomography imaging, such as ^{99m}Tc, I^{123}, and F^{18}-labeled annexin V[49−53] or near-infrared fluorophore-labeled fluorescent probes for optical imaging.[54−57] While these radiotracer-based imaging techniques are useful for some applications, they cannot provide sufficient anatomical resolution for detection of cartilage defects, and some (radiotracers) are associated with radiation exposure. Fluorescently labeled probes have also been used for imaging cell death in anatomical regions other than cartilage.[54−57] However, to date, optical imaging approaches do not provide sufficient anatomical resolution or tissue penetration for stem cell depiction in arthritic joints and are not established for clinical applications. Our choice to create/use an MRI probe circumvents many of these difficulties. Not only is MRI the major imaging modality for evaluation of joints in patients, making the technique directly clinically translatable, but it also provides direct visualization of cartilage defects with no associated ionizing radiation. Additionally, our approach eliminates the need for intravenous injection of the probe.[29,54,58,59] This is required by most MRI-based techniques but is of limited value for evaluation of cell transplants in cartilage defects due to the low or absent vascularization of cartilage. Intravenous contrast agent delivery also makes it difficult to evaluate whether an increasing MRI signal enhancement at a target site is due to increasing contrast agent concentrations or actual activation. We chose delivery *via* direct intra-articular injection of a defined dose and concentration of our C-SNAM probe to ensure that any increase in MR signal in the evaluated cartilage defects was either due to contrast agent retention or increased contrast agent relaxivity, both of which indicate caspase activation. Another advantage is that the required contrast agent doses are very low, thereby minimizing any systemic side effects.

Recently described alternative MR techniques for imaging stem cell death utilized pH-sensitive alginate-based nanosensors[28] and MR-detectable peptides and proteins.[58,59,61] The pH-sensitive alginate-based nanosensor technique is suitable only for cells in hydrogel and not for cells that have been injected directly into the joint or that have migrated elsewhere; this technique may also provide a false indication of cell death due to hydrogel material breakdown or change in pH of the surrounding environment.[60] Other MR-detectable peptides and proteins have been designed for detection of the anionic phospholipid phosphatidylserines.[58,59,61] However, the delivery of these large molecular contrast agents to target sites was limited, thereby limiting the sensitivity of this approach.[59] In addition, systemically applied protein-based probes may trigger immune reactions, thereby limiting repetitive administrations. All previous approaches to detect cell death with activatable MRI biomarkers were hampered by the limited sensitivity of MRI for detecting small changes in relaxivity (MR signal effect) between nonactivated and activated probes. Rather than relying on caspase-3-induced changes in relaxivity alone, we controlled and enhanced differences in MRI signal between viable and apoptotic MASI by direct intra-articular C-SNAM delivery and by using the nanoaggregation properties of our probe to increase probe retention in apoptotic MASI. We could iteratively improve the design of our probe to maximize both sensitivity and specificity by

exchanging Gd with iron oxide or manganese backbones, designing bifunctional probes for combined MRI plus radiotracer or fluorescent imaging, and adding approaches for further enhanced *in vivo* nanoaggregation. Of note, every aspect of our probe has been developed with safety in mind (clinical MR imaging approach, nonimmunogenic clinically used Gd-chelate, clinically established delivery mode, rapid elimination of the probe, *etc.*), making it possible to rapidly translate our probe into the clinic.

CONCLUSION

In summary, we developed a novel, clinically translatable approach for *in vivo* detection of stem cell apoptosis with a caspase-3 activatable contrast agent for MR imaging. This novel approach may be useful for *in vivo* monitoring of the viability of transplanted stem cells and facilitating the development of successful cartilage regeneration techniques. This may enable us to diagnose stem cell transplant failures at an early stage and provide a new imaging biomarker that could help to assign recipients with failing transplants to early interventions or alternative treatment options. The described enhanced relaxivity and retention (ERR effect) of activatable nanoaggregation MRI probes could be used as a platform technology for monitoring specific enzyme activities of other cell transplants and other disease processes in the future.

MATERIALS AND METHODS

Synthesis of C-SNAM Substrate and Analytical *In Vitro* Characterization. We generated C-SNAM by a combination of solution-phase and solid-phase syntheses.[62] After chelation with Gd^{3+} at pH 6.5 at room temperature overnight, C-SNAM was purified by semi-prepared HPLC and obtained as a light yellow powder after lyophilization. The purity of C-SNAM was characterized by analytical HPLC (Dionex Corporation). The compound was identified by matrix-assisted laser desorption/ionization mass spectroscopic analysis and further confirmed by HRMS.

To determine whether C-SNAM is a substrate for cleaved caspase-3, C-SNAM (200 μM) was incubated with human recombinant caspase-3 (50 nM, R&D systems), and the reaction was monitored by using HPLC and by measuring the molecular weight with HRMS. The nanoparticle size of GdNPs was measured with DLS and TEM. To prepare samples for TEM, a 10 μL solution of C-SNAM (200 μM), which had been incubated with caspase-3 (50 nM) in enzyme buffer overnight, was loaded onto a carbon-coated, 400 mesh copper grid (SPI Supplies) and allowed to remain for a few minutes. Excess fluid was removed from the grid. The same grid was washed with 10 μL of ultrapure water, and the excess liquid was removed with kimwipes. The grid was air-dried, and the last traces of solvent were further removed under vacuum. The TEM micrographs and EDX spectroscopy analyses were obtained on an FEI Tecnai G2 F20 X-TWIN transmission electron microscope *via* standard procedures. The r_1 relaxivity of the C-SNAM Gd probe before and after incubation with caspase-3 (50 nM, overnight) in enzyme buffer was obtained by measuring the relaxation time T_1 on a 1 T MR scanner (ICON, Bruker BioSpin Corp.), using a standard inversion recovery fast spin−echo sequence. Relaxation rates (R_1) were determined as $1/T_1$. Longitudinal relaxivities (r_1, a unit of $mM^{-1} \cdot s^{-1}$) were calculated as the slope of R_1 *versus* [Gd] after determination of true Gd concentration for each sample by the ICP-MS (Nu plasma AttoM high-resolution ICP-MS) measurement. T_1-weighted MR images were performed on a 1 T MR scanner (ICON, Bruker BioSpin Corp.) using a T_1-weighted FLASH sequence (TR = 161, TE = 6, FOV = 4 × 4, flip angle = 30, matrix = 256 × 256, slice thickness = 1 mm, number of averages = 5) and a series of inversion recovery fast spin−echo scans, identical in all aspects (TR 6000 ms, TE minimum, field of view = 6 cm, slice thickness = 2 mm, matrix = 128 × 128, NEX 1) except for the inversion time (TI) which was varied as follows: 4000, 2400, 1200, 800, 600, 400, 300, 200, 100, and 50 ms. For quantitative data analysis, MR signal intensities were extracted from each of the samples at each of the TI times by manual region of interest placement. Signal intensity *versus* TI relationships were fit to the following exponential T_1 recovery model by nonlinear least-squares regression: $SI(TI) = S_0[1 - 2^*\exp(-TI/T_1) + \exp(-TR/T_1)]$.

***In Vitro* Evaluations of Stem Cell Apoptosis.** rASCs were harvested and extracted from the abdominal fat pad of nude rats as described previously.[63] rASCs were grown in DMEM media supplemented with 10% stem cell qualified FBS and 100 U/mL penicillin/100 μg/mL streptomycin and subcultured at 80−90% confluency up to five passages. Medium was changed three times a week. Cells at passage 5 were used for all experiments.

To enable noninvasive assessment of stem cell viability, we transduced rASCs with a lentiviral vector construct of the firefly luciferase reporter gene and enhanced green fluorescent protein (FLuc-eGFP), controlled by the constitutively active cytomegalovirus (CMV) promoter. For viral transduction, rASCs were cultured on 10 cm^2 plastic dishes at 50−70% confluency and infected with concentrated CMV-FLUC-eGFP lentivirus particles (kindly donated by Dr. Paulmurugan, Stanford University) in medium containing 8 mg/mL Polybrene (Sigma) for 48 h. Fluorescence-activated cell sorting was used to create a pure population of transduced cells by separating eGFP-expressing cells.

To induce rASC apoptosis, 5×10^5 FLuc-eGFP-transfected rASCs were incubated with 0.5 mg/mL of MMC (Sigma-Aldrich) in DMEM media for 1 h. The cells were washed with PBS and incubated in FBS supplemented DMEM media overnight. Cell viability or apoptosis was confirmed by incubating rASCs with D-Luciferin to determine FLUC activity of the cells with bioluminescent imaging (IVIS Spectrum, PerkinElmer).

In order to confirm the concept of apoptosis detection *via* C-SNAM activation and to determine the C-SNAM optimal dose for subsequent *in vivo* experiments, triplicate samples of 3×10^6 MMC-treated and untreated FLuc-eGFP-transfected MMC-treated and untreated rASCs were incubated with PBS, Gd-DOTA, and C-SNAM probe at concentrations of 0, 250, 500, and 1000 μM overnight. All cell samples underwent MR imaging on a 1 T MR scanner (ICON, Bruker BioSpin Corp.) using a T_1-weighted FLASH sequence (TR = 161 ms, TE = 6 ms, FOV = 4 × 4, flip angle = 30, matrix = 256 × 256, slice thickness = 1 mm, number of averages = 5) and a series of the T_1-weighted FLASH sequences (TR = 1200, 600, 400, 300, 200, 100, 50, 27 ms, TE = 8.8 ms, FOV = 4 × 4 cm, flip angle = 20, matrix = 128 × 256, slice thickness = 1 mm, number of averages = 1) to calculate T_1 relaxation time maps using the saturation curve fitting function of the ParaVision software (Bruker BioSpin Corp.). T_1 relaxation times of all cell samples were measured on these T_1 maps by one investigator (H.N.), using operator-defined regions of interest.

Caspase-3 activation of MMC-exposed cells was confirmed by immunofluorescent staining. After rASC samples were blocked with PBS containing 5% goat serum and 2.5% BSA (blocking buffer), samples were incubated at 4 °C with a cleaved caspase-3 primary antibody (Cell Signaling Technology Inc.) for 2 h, followed by a 2 h incubation with an anti-rabbit IgG(HL) F(ab')2 fragment Alex Fluor 488 secondary antibody (Cell Signaling Technology Inc.). Samples were then mounted with ProLong Hold antifade reagent with DAPI (Invitrogen). The SensoLyte homogenous AMC caspase-3/7 kit (AnaSpec) was used to quantify the cleaved caspase-3 in MMC-treated cells and untreated

controls. According to the manufacturer's instructions, the substrate Ac-DEVD-AMC was used to generate an AMC fluorophore when caspase-3/7 was cleaved. The AMC fluorophore was detected using a fluorometer (ex/em = 354 nm/442 nm). The number of cells that contained activated caspase-3 was quantified with the Vybrant FAM caspase-3/7 assay kit, which is based on the affinity of active caspases with a fluorescent inhibitor of caspases (FLICA). Cell samples are incubated with the propidium iodide and FLICA reagent (according to the FLICA kit instruction) for 1 h, then washed and analyzed through flow cytometry. The FLICA reagent is a conjugate of a caspase-specific amino acid sequence with a fluoromethyl ketone moiety that can react covalently with a cysteine in caspases. In addition, a carboxyfluorescein group (FAM) is attached as a reporter for flow cytometry (ex/em = 488/530).

***In Vivo* Imaging of Stem Cell Apoptosis.** The study was approved by the committee on animal research at our institution. Athymic rats were chosen for this study because the size of the rodents was adequate for MR and BLI and the use of immuno-compromised animals excluded transplant rejection as a possible confounding variable.

In vivo imaging studies were performed in five nude athymic female Harlan rats, which received either transplants of viable rASC (n = 5 knees) or apoptotic rASC (n = 5 knees) in osteochondral defects of the distal femur. A circular osteochondral defect (diameter = 2 mm, depth = 1 mm) was created in the trochlear groove of the distal femur with a microdrill (Flash DP Tabletop Micromotor, DBI America Corp, FL, USA) under inhalation anesthesia. Viable FLUC-eGFP-transduced rASCs (5×10^5) were implanted into the right knee joint, and MMC-treated FLUC-eGFP-transduced rASCs were implanted into the left knee joint using an agarose-based scaffold (1 μL, type VII, Sigma-Aldrich, St Louis, MO, USA).

Twenty-four hours after cell implantation, experimental and control groups underwent MR imaging of both knee joints on a 1 T MR scanner (ICON, Bruker BioSpin Corp.) before and at 30 min, 3 h, and 24 h after intra-articular injections of approximately 40 μL of the C-SNAM Gd probe at a concentration of 500 μM. Knee joints were evaluated with a sagittal T_1-weighted FLASH sequence for depiction of MASI (repetition time, TR = 160 ms, echo time, TE = 8 ms, matrix = 256 × 256, acquisition = 20) as well as a corresponding FLASH sequence with lower anatomical resolution and multiple TRs (TR 1200, 600, 400, 300, 200, 100, 50, 27 ms, TE = 8 ms, matrix = 128 × 256, acquisition = 1) for T_1 quantification. All MR images were obtained with a field of view (FOV) of 4 × 4 cm and a slice thickness of 1 mm. T_1 relaxation time maps were generated with the ParaVision software (Bruker BioSpin Corp.), and T_1 relaxation times of all MASI were measured on these T_1 maps by one investigator (H.N.).

Viability or apoptosis of transplanted FLuc-eGFP-transfected rASCs was confirmed with bioluminescent imaging (IVIS Spectrum, PerkinElmer). Immediately and 24 h after cells implantation, animals underwent BLI imaging of both knee joints after intra-articular injection of 60 μL of D-Luciferin (30 mg/mL).

After completion of all imaging experiments, the animals were sacrificed and knee joints were processed for immunofluorescent stains for detection of cleaved caspase-3 and confirmation of apoptosis. Knee joints were explanted, dissected, and placed in Cal-Rite (Fisher Scientific), dehydrated through graded alcohol washes (70, 95, and 100%) and xylene (EMD, Millipore, USA), embedded in paraffin, and sliced into 5 μm thick tissue slices on glass slides. The slides were dewaxed to undergo immunofluorescent staining to detect presence of cleaved caspase-3 in the implants.

Statistical Analysis. We used ParaVision software (Bruker BioSpin Corp.) to calculate the T_1 relaxation times and Living Image software to calculate the photon influx of the BLI images. For the statistical analysis of T_1 relaxation times, data, and photon influx of BLI images, we employed a Student's t test for the comparison between viable and apoptotic samples of *in vitro* and *in vivo* experiments. P values <0.05 were considered to be statistically significant. We used Prism 6 (Prism GraphPad Software, Inc., San Diego) to perform the statistical tests.

Conflict of Interest: The authors declare no competing financial interest.

Acknowledgment. The data presented in the paper was acquired on instruments in the Stanford School of Medicine small animal imaging facility shared service center. We would like to acknowledge Danielle Beecham for her help with manuscript editing. We also like to thank R. Paulmurugan, T. Veerapazham, and K. Foygel for the kind donation of the lentiviral vector construct of the CMV-FLuc-eGFP. This work was supported by NIH Grant No. 2R01AR054458-05 from the National Institute of Arthritis and Musculoskeletal and Skin Diseases, National Institute of Cancer (NCI) Stanford CCNE-T grant (U54CA151459), and In vivo Cellular and Molecular Imaging Centers grant (P50CA114747). R.C.'s funding was provided by the Stanford Medical Scholars Fellowship Program.

Supporting Information Available: HRMS of cyclized products of macrocycles I and II; DLS analysis of C-SNAM following incubation with caspase-3; EDX spectroscopy analysis of the nanoparticles; *in vivo* MRI of viable and apoptotic rASC implants in different time points. This material is available free of charge *via* the Internet at http://pubs.acs.org.

REFERENCES AND NOTES

1. Total number of discharges for knee arthoplastly in 2010 in U.S.; http://hcupnet.ahrq.gov/HCUPnet.jsp (accessed October 16, 2012).
2. Brooks, P. M. Impact of Osteoarthritis on Individuals and Society: How Much Disability? Social Consequences and Health Economic Implications. *Curr. Opin. Rheumatol.* **2002**, *14*, 573–577.
3. Gupta, S.; Hawker, G. A.; Laporte, A.; Croxford, R.; Coyte, P. C. The Economic Burden of Disabling Hip and Knee Osteoarthritis (OA) from the Perspective of Individuals Living with This Condition. *Rheumatology (Oxford)* **2005**, *44*, 1531–1537.
4. Nejadnik, H.; Hui, J. H.; Feng Choong, E. P.; Tai, B. C.; Lee, E. H. Autologous Bone Marrow-Derived Mesenchymal Stem Cells *versus* Autologous Chondrocyte Implantation: An Observational Cohort Study. *Am. J. Sports Med.* **2010**, *38*, 1110–1116.
5. Kurtz, S.; Ong, K.; Lau, E.; Mowat, F.; Halpern, M. Projections of Primary and Revision Hip and Knee Arthroplasty in the United States from 2005 to 2030. *J. Bone Joint Surg. Am.* **2007**, *89*, 780–785.
6. Daniel, J.; Ziaee, H.; Kamali, A.; Pradhan, C.; Band, T.; McMinn, D. J. Ten-Year Results of a Double-Heat-Treated Metal-on-Metal Hip Resurfacing. *J. Bone Joint Surg. Br.* **2010**, *92*, 20–27.
7. Fary, C.; Thomas, G. E.; Taylor, A.; Beard, D.; Carr, A.; Glyn-Jones, S. Diagnosing and Investigating Adverse Reactions in Metal on Metal Hip Implants. *Br. Med. J.* **2011**, *343*, d7441.
8. Murray, D. W.; Grammatopoulos, G.; Pandit, H.; Gundle, R.; Gill, H. S.; McLardy-Smith, P. The Ten-Year Survival of the Birmingham Hip Resurfacing: An Independent Series. *J. Bone Joint Surg. Br.* **2012**, *94*, 1180–1186.
9. Jorgensen, C.; Gordeladze, J.; Noel, D. Tissue Engineering through Autologous Mesenchymal Stem Cells. *Curr. Opin. Biotechnol.* **2004**, *15*, 406–410.
10. Anderson, J. A.; Little, D.; Toth, A. P.; Moorman, C. T., III; Tucker, B. S.; Ciccotti, M. G.; Guilak, F. Stem Cell Therapies for Knee Cartilage Repair: The Current Status of Preclinical and Clinical Studies. *Am. J. Sports Med.* **2014**, *42*, 2253–2261.
11. Steinert, A. F.; Ghivizzani, S. C.; Rethwilm, A.; Tuan, R. S.; Evans, C. H.; Noth, U. Major Biological Obstacles for Persistent Cell-Based Regeneration of Articular Cartilage. *Arthritis Res. Ther.* **2007**, *9*, 213.
12. Koga, H.; Engebretsen, L.; Brinchmann, J. E.; Muneta, T.; Sekiya, I. Mesenchymal Stem Cell-Based Therapy for Cartilage Repair: A Review. *Knee Surg. Sports Traumatol. Arthrosc.* **2009**, *17*, 1289–1297.

13. Hagiwara, M.; Shen, B.; Chao, L.; Chao, J. Kallikrein-Modified Mesenchymal Stem Cell Implantation Provides Enhanced Protection Against Acute Ischemic Kidney Injury by Inhibiting Apoptosis and Inflammation. *Hum. Gene Ther.* **2008**, *19*, 807–819.
14. Allen, D. B.; Maguire, J. J.; Mahdavian, M.; Wicke, C.; Marcocci, L.; Scheuenstuhl, H.; Chang, M.; Le, A. X.; Hopf, H. W.; Hunt, T. K. Wound Hypoxia and Acidosis Limit Neutrophil Bacterial Killing Mechanisms. *Arch. Surg.* **1997**, *132*, 991–996.
15. Hyun, J.; Grova, M.; Nejadnik, H.; Lo, D.; Morrison, S.; Montoro, D.; Chung, M.; Zimmermann, A.; Walmsley, G. G.; Lee, M.; Daldrup-Link, H.; Wan, D. C.; Longaker, M. T. Enhancing *In Vivo* Survival of Adipose-Derived Stromal Cells through Bcl-2 Overexpression Using a Minicircle Vector. *Stem Cells Transl. Med.* **2013**, *2*, 690–702.
16. Broughton, G., II; Janis, J. E.; Attinger, C. E. Wound Healing: An Overview. *Plast. Reconstr. Surg.* **2006**, *117*, 1e-S–32e-S.
17. Zhang, M.; Methot, D.; Poppa, V.; Fujio, Y.; Walsh, K.; Murry, C. E. Cardiomyocyte Grafting for Cardiac Repair: Graft Cell Death and Anti-death Strategies. *J. Mol. Cell Cardiol.* **2001**, *33*, 907–921.
18. Wu, Y.; Chen, L.; Scott, P. G.; Tredget, E. E. Mesenchymal Stem Cells Enhance Wound Healing through Differentiation and Angiogenesis. *Stem Cells* **2007**, *25*, 2648–2659.
19. Sareen, D.; Ebert, A. D.; Heins, B. M.; McGivern, J. V.; Ornelas, L.; Svendsen, C. N. Inhibition of Apoptosis Blocks Human Motor Neuron Cell Death in a Stem Cell Model of Spinal Muscular Atrophy. *PLoS One* **2012**, *7*, e39113.
20. Pearl, J. I.; Lee, A. S.; Leveson-Gower, D. B.; Sun, N.; Ghosh, Z.; Lan, F.; Ransohoff, J.; Negrin, R. S.; Davis, M. M.; Wu, J. C. Short-Term Immunosuppression Promotes Engraftment of Embryonic and Induced Pluripotent Stem Cells. *Cell Stem Cell* **2011**, *8*, 309–317.
21. Imai, Y.; Adachi, Y.; Shi, M.; Shima, C.; Yanai, S.; Okigaki, M.; Yamashima, T.; Kaneko, K.; Ikehara, S. Caspase Inhibitor ZVAD-Fmk Facilitates Engraftment of Donor Hematopoietic Stem Cells in Intra-bone Marrow-Bone Marrow Transplantation. *Stem Cells Dev.* **2010**, *19*, 461–468.
22. Hyun, J. S.; Tran, M. C.; Wong, V. W.; Chung, M. T.; Lo, D. D.; Montoro, D. T.; Wan, D. C.; Longaker, M. T. Enhancing Stem Cell Survival *in Vivo* for Tissue Repair. *Biotechnol. Adv.* **2013**, *31*, 736–743.
23. Laflamme, M. A.; Chen, K. Y.; Naumova, A. V.; Muskheli, V.; Fugate, J. A.; Dupras, S. K.; Reinecke, H.; Xu, C.; Hassanipour, M.; Police, S.; O'Sullivan, C.; Collins, L.; Chen, Y.; Minami, E.; Gill, E. A.; Ueno, S.; Yuan, C.; Gold, J.; Murry, C. E. Cardiomyocytes Derived from Human Embryonic Stem Cells in Pro-survival Factors Enhance Function of Infarcted Rat Hearts. *Nat. Biotechnol.* **2007**, *25*, 1015–1024.
24. Karoubi, G.; Ormiston, M. L.; Stewart, D. J.; Courtman, D. W. Single-Cell Hydrogel Encapsulation for Enhanced Survival of Human Marrow Stromal Cells. *Biomaterials* **2009**, *30*, 5445–5455.
25. Abu-Qare, A. W.; Abou-Donia, M. B. Biomarkers of Apoptosis: Release of Cytochrome *c*, Activation of Caspase-3, Induction of 8-Hydroxy-2′-deoxyguanosine, Increased 3-Nitrotyrosine, and Alteration of P53 Gene. *J. Toxicol. Environ. Health, Part B* **2001**, *4*, 313–332.
26. Ding, C.; Cicuttini, F.; Jones, G. How Important Is MRI for Detecting Early Osteoarthritis? *Nat. Clin. Pract. Rheumatol.* **2008**, *4*, 4–5.
27. Link, T. M.; Stahl, R.; Woertler, K. Cartilage Imaging: Motivation, Techniques, Current and Future Significance. *Eur. Radiol.* **2007**, *17*, 1135–1146.
28. Chan, K. W.; Liu, G.; Song, X.; Kim, H.; Yu, T.; Arifin, D. R.; Gilad, A. A.; Hanes, J.; Walczak, P.; van Zijl, P. C.; Bulte, J. W.; McMahon, M. T. MRI-Detectable pH Nanosensors Incorporated into Hydrogels for *In Vivo* Sensing of Transplanted-Cell Viability. *Nat. Mater.* **2013**, *12*, 268–275.
29. Dash, R.; Chung, J.; Chan, T.; Yamada, M.; Barral, J.; Nishimura, D.; Yang, P. C.; Simpson, P. C. A Molecular MRI Probe To Detect Treatment of Cardiac Apoptosis *in Vivo*. *Magn. Reson. Med.* **2011**, *66*, 1152–1162.
30. Mulder, W. J.; Strijkers, G. J.; van Tilborg, G. A.; Griffioen, A. W.; Nicolay, K. Lipid-Based Nanoparticles for Contrast-Enhanced MRI and Molecular Imaging. *NMR Biomed.* **2006**, *19*, 142–164.
31. Kielar, F.; Tei, L.; Terreno, E.; Botta, M. Large Relaxivity Enhancement of Paramagnetic Lipid Nanoparticles by Restricting the Local Motions of the Gd(III) Chelates. *J. Am. Chem. Soc.* **2010**, *132*, 7836–7837.
32. Ye, D.; Pandit, P.; Kempen, P.; Lin, J.; Xiong, L.; Sinclair, R.; Rutt, B.; Rao, J. Redox-Triggered Self-Assembly of Gadolinium-Based MRI Probes for Sensing Reducing Environment. *Bioconjugate Chem.* **2014**, *25*, 1526–1536.
33. Ye, D.; Shuhendler, A. J.; Pandit, P.; Brewer, K. D.; Tee, S. S.; Cui, L.; Tikhomirov, G.; Rutt, B.; Rao, J. Caspase-Responsive Smart Gadolinium-Based Contrast Agent for Magnetic Resonance Imaging of Drug-Induced Apoptosis. *Chem. Sci.* **2014**, *4*, 3845–3852.
34. Koga, H.; Muneta, T.; Ju, Y. J.; Nagase, T.; Nimura, A.; Mochizuki, T.; Ichinose, S.; von der Mark, K.; Sekiya, I. Synovial Stem Cells Are Regionally Specified According to Local Microenvironments after Implantation for Cartilage Regeneration. *Stem Cells* **2007**, *25*, 689–696.
35. Park, J.; Gelse, K.; Frank, S.; von der Mark, K.; Aigner, T.; Schneider, H. Transgene-Activated Mesenchymal Cells for Articular Cartilage Repair: A Comparison of Primary Bone Marrow-, Perichondrium/Periosteum- and Fat-Derived Cells. *J. Gene Med.* **2006**, *8*, 112–125.
36. Jurgens, W. J.; Kroeze, R. J.; Zandieh-Doulabi, B.; van Dijk, A.; Renders, G. A.; Smit, T. H.; van Milligen, F. J.; Ritt, M. J.; Helder, M. N. One-Step Surgical Procedure for the Treatment of Osteochondral Defects with Adipose-Derived Stem Cells in a Caprine Knee Defect: A Pilot Study. *BioRes. Open Access* **2013**, *2*, 315–325.
37. Tang, C.; Jin, C.; Du, X.; Chao, Y.; Min, B. H. M. P.; Xu, Y.; Wang, L. An Autologous Bone Marrow Mesenchymal Stem Cell-Derived Extracellular Matrix Scaffold Applied with Bone Marrow Stimulation for Cartilage Repair. *Tissue Eng., Part A* **2014**, *2*, 2455–2462.
38. McGinley, L. M.; McMahon, J.; Stocca, A.; Duffy, A.; Flynn, A.; O'Toole, D.; O'Brien, T. Mesenchymal Stem Cell Survival in the Infarcted Heart Is Enhanced by Lentivirus Vector-Mediated Heat Shock Protein 27 Expression. *Hum. Gene Ther.* **2013**, *24*, 840–851.
39. Liang, Y.; Walczak, P.; Bulte, J. W. The Survival of Engrafted Neural Stem Cells within Hyaluronic Acid Hydrogels. *Biomaterials* **2013**, *34*, 5521–5529.
40. Marlovits, S.; Aldrian, S.; Wondrasch, B.; Zak, L.; Albrecht, C.; Welsch, G.; Trattnig, S. Clinical and Radiological Outcomes 5 Years after Matrix-Induced Autologous Chondrocyte Implantation in Patients with Symptomatic, Traumatic Chondral Defects. *Am. J. Sports Med.* **2012**, *40*, 2273–2280.
41. Trattnig, S.; Domayer, S.; Welsch, G. W.; Mosher, T.; Eckstein, F. MR Imaging of Cartilage and Its Repair in the Knee—A Review. *Eur. Radiol.* **2009**, *19*, 1582–1594.
42. Henning, T. D.; Wendland, M. F.; Golovko, D.; Sutton, E. J.; Sennino, B.; Malek, F.; Bauer, J. S.; McDonald, D. M.; Daldrup-Link, H. Relaxation Effects of Ferucarbotran-Labeled Mesenchymal Stem Cells at 1.5T and 3T: Discrimination of Viable from Lysed Cells. *Magn. Reson. Med.* **2009**, *62*, 325–332.
43. Boddington, S. E.; Sutton, E. J.; Henning, T. D.; Nedopil, A. J.; Sennino, B.; Kim, A.; Daldrup-Link, H. E. Labeling Human Mesenchymal Stem Cells with Fluorescent Contrast Agents: The Biological Impact. *Mol. Imaging Biol.* **2010**, *13*, 3–9.
44. Sutton, E. J.; Henning, T. D.; Boddington, S.; Demos, S.; Krug, C.; Meier, R.; Kornak, J.; Zhao, S.; Baehner, R.; Sharifi, S.; Daldrup-Link, H. *In Vivo* Magnetic Resonance Imaging and Optical Imaging Comparison of Viable and Nonviable Mesenchymal Stem Cells with a Bifunctional Label. *Mol. Imaging* **2010**, *9*, 278–290.
45. Henning, T. D.; Gawande, R.; Khurana, A.; Tavri, S.; Mandrussow, L.; Golovko, D.; Horvai, A.; Sennino, B.; McDonald, D.; Meier, R.; Wendland, M.; Derugin, N.; Link, T. M.; Daldrup-Link, H. E. Magnetic Resonance Imaging of

Ferumoxide-Labeled Mesenchymal Stem Cells in Cartilage Defects: *In Vitro* and *In Vivo* Investigations. *Mol. Imaging* **2012**, *11*, 197–209.
46. Khurana, A.; Nejadnik, H.; Gawande, R.; Lin, G.; Lee, S.; Messing, S.; Castaneda, R.; Derugin, N.; Pisani, L.; Lue, T. F.; Daldrup-Link, H. E. Intravenous Ferumoxytol Allows Noninvasive MR Imaging Monitoring of Macrophage Migration into Stem Cell Transplants. *Radiology* **2012**, *264*, 803–811.
47. Khurana, A.; Nejadnik, H.; Chapelin, F.; Lenkov, O.; Gawande, R.; Lee, S.; Gupta, S. N.; Aflakian, N.; Derugin, N.; Messing, S.; Lin, G.; Lue, T. F.; Pisani, L.; Daldrup-Link, H. E. Ferumoxytol: A New, Clinically Applicable Label for Stem-Cell Tracking in Arthritic Joints with MRI. *Nanomedicine* **2013**, *8*, 1969–1983.
48. Khurana, A.; Chapelin, F.; Beck, G.; Lenkov, O. D.; Donig, J.; Nejadnik, H.; Messing, S.; Derugin, N.; Chan, R. C.; Gaur, A.; Sennino, B.; McDonald, D. M.; Kempen, P. J.; Tikhomirov, G. A.; Rao, J.; Daldrup-Link, H. E. Iron Administration before Stem Cell Harvest Enables MR Imaging Tracking after Transplantation. *Radiology* **2013**, *269*, 186–197.
49. Blankenberg, F. G.; Katsikis, P. D.; Tait, J. F.; Davis, R. E.; Naumovski, L.; Ohtsuki, K.; Kopiwoda, S.; Abrams, M. J.; Darkes, M.; Robbins, R. C.; Maecker, H. T.; Strauss, H. W. *In Vivo* Detection and Imaging of Phosphatidylserine Expression During Programmed Cell Death. *Proc. Natl. Acad. Sci. U.S.A.* **1998**, *95*, 6349–6354.
50. Tait, J. F.; Smith, C.; Blankenberg, F. G. Structural Requirements for *In Vivo* Detection of Cell Death with 99mtc-Annexin V. *J. Nucl. Med.* **2005**, *46*, 807–815.
51. Lahorte, C. M.; Vanderheyden, J. L.; Steinmetz, N.; Van de Wiele, C.; Dierckx, R. A.; Slegers, G. Apoptosis-Detecting Radioligands: Current State of the Art and Future Perspectives. *Eur. J. Nucl. Med. Mol. Imaging* **2004**, *31*, 887–919.
52. Blankenberg, F. To Scan or Not To Scan, It Is a Question of Timing: Technetium-99m-Annexin V Radionuclide Imaging Assessment of Treatment Efficacy after One Course of Chemotherapy. *Clin. Cancer Res.* **2002**, *8*, 2757–2758.
53. Kartachova, M.; van Zandwijk, N.; Burgers, S.; van Tinteren, H.; Verheij, M.; Valdes Olmos, R. A. Prognostic Significance of ^{99m}Tc Hynic-Rh-Annexin V Scintigraphy during Platinum-Based Chemotherapy in Advanced Lung Cancer. *J. Clin. Oncol.* **2007**, *25*, 2534–2539.
54. Edgington, L. E.; Berger, A. B.; Blum, G.; Albrow, V. E.; Paulick, M. G.; Lineberry, N.; Bogyo, M. Noninvasive Optical Imaging of Apoptosis by Caspase-Targeted Activity-Based Probes. *Nat. Med.* **2009**, *15*, 967–973.
55. Schoenberger, J.; Bauer, J.; Moosbauer, J.; Eilles, C.; Grimm, D. Innovative Strategies in *In Vivo* Apoptosis Imaging. *Curr. Med. Chem.* **2008**, *15*, 187–194.
56. Khanna, D.; Hamilton, C. A.; Bhojani, M. S.; Lee, K. C.; Dlugosz, A.; Ross, B. D.; Rehemtulla, A. A Transgenic Mouse for Imaging Caspase-Dependent Apoptosis within the Skin. *J. Invest. Dermatol.* **2010**, *130*, 1797–1806.
57. Hanshaw, R. G.; Lakshmi, C.; Lambert, T. N.; Johnson, J. R.; Smith, B. D. Fluorescent Detection of Apoptotic Cells by Using Zinc Coordination Complexes with a Selective Affinity for Membrane Surfaces Enriched with Phosphatidylserine. *ChemBioChem* **2005**, *6*, 2214–2220.
58. Zhao, M.; Beauregard, D. A.; Loizou, L.; Davletov, B.; Brindle, K. M. Non-invasive Detection of Apoptosis Using Magnetic Resonance Imaging and a Targeted Contrast Agent. *Nat. Med.* **2001**, *7*, 1241–1244.
59. Krishnan, A. S.; Neves, A. A.; de Backer, M. M.; Hu, D. E.; Davletov, B.; Kettunen, M. I.; Brindle, K. M. Detection of Cell Death in Tumors by Using MR Imaging and a Gadolinium-Based Targeted Contrast Agent. *Radiology* **2008**, *246*, 854–862.
60. Ziv, K.; Gambhir, S. S. Bioengineering and Regenerative Medicine: Keeping Track. *Nat. Mater.* **2013**, *12*, 180–181.
61. Jung, H. I.; Kettunen, M. I.; Davletov, B.; Brindle, K. M. Detection of Apoptosis Using the C2A Domain of Synaptotagmin I. *Bioconjugate Chem.* **2004**, *15*, 983–987.
62. Ye, D.; Shuhendler, A. J.; Cui, L.; Tong, L.; Tee, S. S.; Tikhomirov, G.; Felsher, D. W.; Rao, J. Bioorthogonal Cyclization-Mediated *In Situ* Self-Assembly of Small-Molecule Probes for Imaging Caspase Activity *in Vivo*. *Nat. Chem.* **2014**, *6*, 519–526.
63. Nejadnik, H.; Castillo, R.; Daldrup-Link, H. E. Magnetic Resonance Imaging and Tracking of Stem Cells. *Methods Mol. Biol.* **2013**, *1052*, 167–176.